LAWRENCE
LIVERMORE
NATIONAL
LABORATORY

LLNL-CONF-697484

Analysis of Edge Stability for Models of Heat Flux Width

M. A. Makowski, C. J. Lasnier, A. W. Leonard, T. H. Osborne

July 13, 2016

22nd International Conference on Plasma Surface Interaction in Controlled Fusion Devices
Rome, Italy
May 30, 2016 through June 3, 2016

Disclaimer

Analysis of Edge Stability for Models of Heat Flux Width

M.A. Makowski[1], C.J. Lasnier[1], A.W. Leonard[2], and T.H. Osborne[2]

[1]*Lawrence Livermore National Laboratory, Livermore, California 94550, USA*
[2]*General Atomics, P.O. Box 85608, San Diego, California 92186-5608, USA*

Abstract:

Detailed measurements of the n_e, T_e, and T_i profiles in the vicinity of the separatrix of ELMing H-mode discharges have been used to examine plasma stability at the extreme edge of the plasma and assess stability dependent models of the heat flux width. The results are not consistent with the critical gradient model, which posits that a ballooning instability determines a gradient scale length related to the heat flux width. This result is not sensitive to the choice of location used to evaluate the stability. It is also found that the results are consistent with the heuristic drift model for the heat flux width. Here the edge pressure gradient scales with plasma density and is proportional to that inferred from the equilibrium, in accordance with the predictions of the theory.

Introduction

The physics determining the heat flux width in the scrape-off layer (SOL) has yet to be firmly established, even though it is an important parameter determining the operational limits in ITER. It is known that at high edge collisionality, the regime common to current day experiments, that the heat flux width scales inversely with the plasma current [1], or equivalently, with the inverse of the poloidal field at the outer midplane ($B_{p,omp}$). When extrapolated to ITER, this scaling law predicts a heat flux width on the order of 1 mm, resulting in heat loads that will exceed material limits. However, the SOL in ITER is projected to be hotter, and thus less collisional, so it is unclear whether this scaling will hold in this regime.

A large number of models have been proposed for heat flux width [2], but two have been the subject of current research. They are the heuristic drift model [3,4,5] and the critical gradient model [6]. The drift model proposes that the grad-B and curvature drifts inject particles into the SOL, half of which transit to the divertor at a flow velocity of $c_s/2$, where c_s is the sound speed. Anomalous electron thermal conduction is invoked to account for the heat transport to the divertor. The model predicts a heat flux width scaling as $(a/R)\rho_p$ where a is the minor radius, R the major radius, and ρ_p is the poloidal ion gyroradius, in good agreement with measurements [7].

Alternatively, the critical gradient model assumes that an MHD mode is destabilized as the edge pressure gradient increases past a critical value. Upon reaching the critical value, the mode grows rapidly, inducing radial transport and clamping the

pressure gradient near the critical value. The critical pressure gradient for the infinite-n ideal ballooning mode is usually taken as a proxy for the stability limit. This is analogous to the process setting the pedestal pressure gradient in the critical gradient model for ELM onset [8], except that in this case the instability is assumed localized to the separatrix rather than the pedestal, thereby establishing a heat flux width characteristic of the pressure gradient scale length at the separatrix.

A stringent test for the critical gradient model is whether the theoretical stability limit scales with the measured value of the poloidal-beta at the outer mid-plane, $\beta_{p,omp}$, since the stability limit should depend strongly on this quantity. Below, we present strong evidence to the contrary: the theoretical stability limit is almost independent of the measured $\beta_{p,omp}$.

A large number of type-I ELMing H-mode discharges with attached outer divertor legs, spanning a wide range of plasma currents (0.5 -1.5 MA), injected powers (NBI: 2-11 MW and ECH: 2-3 MW), and densities (0.090-0.666 x 10^{20} m^{-3}) have been analyzed. In each instance, between-ELM profiles of n_e, T_e, and P_e, obtained from a high spatial resolution Thomson scattering system, and T_i profiles, obtained from charge exchange recombination measurements, were generated and used to construct a kinetic EFIT [9], which was then used to perform edge stability analysis with the BALOO code [10]. These profiles were then used to obtain quantities at the separatrix, which then provided a measure of $\beta_{p,omp}$. For comparison, the divertor heat flux profiles were characterized by the Eich-formulation [1] for each time slice in the data set.

Stability Analysis for the Critical Gradient Model

The infinite-n, ideal ballooning mode (IBM) critical pressure gradient limit, as computed by the BALOO code [10], is used as a proxy for the stability limit at the separatrix. Figure 1a shows a typical result from the BALOO code, plotting the pressure gradient stability boundary as a function of normalized poloidal flux, ψ. The computation only extends to $\psi = 0.998$, and is extrapolated incrementally to $\psi = 1$ to obtain the theoretical critical pressure gradient at the separatrix.

For many of the low current discharges examined, the extreme edge ($\psi > 0.98$) was second stable (. In this case the pressure gradient was obtained from the envelope of the *s-p'* curves, where *s* is the shear and *p'* is the pressure gradient, for the flux surfaces nearest the separatrix as shown in Fig. 1b. This limit is generally a slightly more conservative estimate of the stability limit as can be seen by comparing the two limits depicted in Figs. 1a and 1b.

Figure 2 is a summary plot of the data, plotting both the measured pressure gradient and the BALOO calculated critical pressure gradient as a function of poloidal-beta at the outer midplane, $\beta_{p,omp}$. The measured pressure gradient is shown in solid

symbols for three different values of plasma current: red-circles for I_p = 0.5 MA, green squares for I_p = 1.0 MA, and blue triangles for I_p = 1.5 MA. The pressure gradient obtained from the envelope of the *s-p'* curves for the flux surfaces nearest the separatrix (Fig. 1b) are depicted by open squares in Fig. 2. Data for I_p = 0.5 MA is relatively sparse as many of the discharges were compromised by high-β instabilities. In all cases, regardless of the choice of stability limit, the measured pressure gradient lies well below the theoretical stability limit, contrary to the expectations of the critical gradient model for the heat flux width. The largest difference occurs at the smallest values of $\beta_{p,omp}$ where the two quantities differ by as much as a factor of 3.

Previously it was reported [11] that the measured pressure gradient was close to the IBM critical gradient. The discharges in the earlier study were generally at high density and $\beta_{p,omp}$ with the exception of the lowest power case (see Fig. 5 of [11]) where the measured pressure gradients decreases with decreasing normalized density (Greenwald fraction) f_{GW}, hinting at the results of this study. This older data has been included in the current study and extended to much lower $f_{GW.}$

Profile Analysis

The above results depend critically on the separatrix value of the measured pressure gradient. However, we find that the result is independent of the method used to identify the separatrix as long as a single method is used. To justify this statement, 6 different methods of identifying the separatrix were compared: 1) standard method of using a tanh-function [12], 2) Te = 60 eV point on a tanh-fit, 3) power balance [13] using a tanh-fit, 4) Te = 60 eV on a hyperbola fit to the pedestal and SOL data, 5) power balance using a hyperbola fit to the pedestal and SOL data, and 6) point of intersection of the asymptotes of a hyperbola fit to the pedestal and SOL data. Figure 3 compares a tanh and hyperbola fit to the T_e data and depicts the separatrix locations obtained by means of methods 2, 4, and 6. The different locations are within +/- 2 mm on another. However, they yield very different estimates of the temperature gradient.

Results of a comparison between the various separatrix identification methods are displayed in Fig. 4, which plots separatrix locations found by means of methods 2-6 versus that from method 1, the standard method. The color-coding is red circles, blue squares, magenta circles, cyan squares, and green triangles for methods 2-6 respectively. From this plot it is evident that the various methods track one another quite well indicating that there is an approximately linear relation with unity slope, differing only in offset between any two of the methods. That is, each method differs only in the relative location of the separatrix in relation to the standard method, being *consistently* higher, lower, or about the same. The net effect of this shift is to respectively increase, decrease, or not affect the measured pressure and pressure gradient. This in turn, scales both the pressure gradient and $\beta_{p,omp}$ axes of Fig. 2, but does not alter the linear relation between them. Further, in order for the measured

pressure gradient to exceed the IBM critical gradient over a significant range of $\beta_{p,omp}$, the location of the separatrix has to be near the top of the pedestal (which is exactly the criteria needed to trigger ELMs in the ePed model [8]). Thus, the exact choice of separatrix is not critical; only a consistent applied measure is needed for our conclusions to hold. Incidentally, we note that all the separatrix locations all occur within a band of +/- 2 mm, which corresponds to about +/- 0.01 in normalized poloidal flux, ψ. With the scatter in the data, it would be difficult to pinpoint the location of "the separatrix" to an accuracy better than these limits.

The ion temperature and density profiles contribute significantly to the total pressure and pressure gradient. This may be seen in Fig. 5a which plots the electron (red circles) and ion (green squares) pressure versus the total pressure, and Fig. 5b which plots the 4 components of the pressure gradient ($n_e\nabla T_e$ (red circles), $T_e\nabla n_e$ (green squares), $n_i\nabla T_i$ (blue upward pointing triangles), and $T_i\nabla n_i$ (cyan downward pointing triangles)) versus the total pressure. The ion pressure, P_i, is the largest contributor to the total pressure, being 3-4 times larger than the electron pressure, P_e. The rise in pressure with P_{tot} occurs primarily from a rapidly increasing density. The electron and ion temperatures also increase with P_{tot}, but only by about a factor of about 2. The largest contributor to the total pressure gradient, ∇P_{tot}, is the ion term $T_i\nabla n_i$. This results from a combination of the high ion separatrix temperature in combination with a relatively steep ion density gradient. The other three terms contribute approximately equally and are about 2-3 times smaller that the $T_i\nabla n_i$ term.

Heuristic Drift Model

The breadth of the data set allows us to examine some of the predictions of the heuristic drift (HD) model [3,4,5], in particular, comparison of estimates of the normalized pressure gradient $\tilde{\alpha}$. Two quantities arise in the theory (Eq. 4 of [4])

$$\tilde{\alpha}_{SOL} = \frac{Rq_{cyl}^2 2(\bar{n}_{20,e}/3)eT_{spitzer}}{\lambda_q B_t^2/2\mu_0} \tag{1}$$

and (as defined in [5])

$$\tilde{\alpha}_{HD} = 0.123 f_{GW}\frac{n_{e,sep}}{\bar{n}}\left(\frac{q_{cyl}RB}{a}P_{sol}\right)^{1/8}\left(1+\kappa^2\right)^{3/2}\left[\frac{2\bar{A}}{1+\bar{Z}}\right]^{-9/16}\left(\frac{Z_{eff}+4}{5}\right)^{1/8} \tag{2}$$

Figure 6a plots $\tilde{\alpha}_{SOL}$ versus the Greenwald fraction, f_{GW}. The data shows $\tilde{\alpha}_{SOL}$ increasing with f_{GW}, with an abrupt increase at $f_{GW} \sim$ 0.4-0.5. These data neatly fit into Fig. 3 of reference [4], and extend the trend to much lower f_{GW}. It has not been

possible to obtain data for f_{GW} > 0.6-0.7 as the outer divertor detaches with a corresponding increase in outboard density. The density increase then relaxes the pedestal and separatrix pressure gradients, α_{sep}.

Additionally, Fig. 6b plots $\tilde{\alpha}_{HD}$ versus α_{efit}, the normalized separatrix pressure gradient obtained from a kinetic EFIT [9] reconstruction. There is a very good correlation between the two. The dotted line is a fit (constrained to pass through zero) to the data and has slope 0.56. Thus the data is well approximated by the relation $\tilde{\alpha}_{HD} \approx \alpha_{efit}/2$. Thus this data is consistent with the predictions of the heuristic drift model.

Discussion

High-resolution measurements of the n_e, T_e, and T_i profiles in the vicinity of the separatrix provide an experimental measure of the pressure profile and its gradient in this region, allowing direct comparison of these quantities with theoretical stability limits. When compared to the predictions of the critical gradient model for the heat flux width, substantial disagreement is found. The measured pressure gradient lies well below the critical pressure gradient found from infinite-n ideal ballooning mode theory. The disagreement is particularly large for the lowest values of $\beta_{p,omp}$. The data show a near linear dependence of the pressure gradient on $\beta_{p,omp}$ at fixed plasma current. The disagreement cannot be attributed to the choice of separatrix location as each method of doing so systematically moves the location to larger or smaller values of major radius, which has the effect of scaling the $\beta_{p,omp}$ axis, and to a lesser extent, ∇P. However, this effect does not alter the relationship between $\beta_{p,omp}$, ∇P, and the theoretical stability limit.

Resistive modes are thought not to have a threshold for instability as ballooning modes do, and so cannot completely be eliminated as an alternative means of providing a stability limit. However, the edge resistivity is high and varies by no more than a factor $2^{3/2}$ = 2.8 across the entire data set. Thus, it is unlikely resistive effects can account for the observed variation in the data.

In contrast to the critical gradient model, the results are found to be quite consistent with the predictions of the heuristic drift model. Here, a density dependence at low f_{GW} (Fig. 6a) is found to be consistent with results of other devices at higher values of f_{GW}. Additionally, the quantity $\tilde{\alpha}_{HD}$ scales linearly with α_{efit}, the separatrix value of α obtained from a kinetic EFIT reconstruction with the result that $\tilde{\alpha}_{HD} \approx \alpha_{efit}/2$ with a high degree of correlation. Despite the heuristic nature of the theory, it has a unique ability to accurately model the data. A more fundamental understanding of the underlying physics is clearly desirable, particularly in regard to the nature of the anomalous electron thermal transport.

Acknowledgements

This work was supported by the U.S. Department of Energy under DE-AC52-07NA27344, DE-FC02-04ER54698, and DE-AC02-09CH11466. DIII-D data shown in this paper can be obtained in digital format by following the links at https://fusion.gat.com/global.D3D_DMP.

References

[1] T. Eich, et al., Phys. Rev. Lett. **107** (2011) 215001.
[2] W. Fundamenski and S. Sipila, Nucl. Fusion **44** (2004) 20.
[3] R.J. Goldston, Nuc. Fusion **52** (2012) 013009.
[4] R.J. Goldston and T. Eich, in: IAEA Fusion Energy Conference, (2012) TH/P4-19.
[5] R.J. Goldston, JNM **463** (2015) 397.
[6] B.N. Rogers, et al., Phys. Rev. Lett. **81** (1998) 4396.
[7] T. Eich, et al., in: IAEA Fusion Energy Conference, (2012) ITER/1-1.
[8] P.B. Snyder, et al., Phys. Plasmas **16** (2009) 056118.
[9] J.L. Luxon, L.G. Davis, Fusion Technol. **8** (Part 2A) (1985) 441.
[10] R.L. Miller, *et al.*, Phys. Plasmas **4** (1997) 1062.
[11] M.A. Makowski, et al., JNM **463**, (2015), 55.
[12] G.D. 12, et al., Phys. Plasmas **5** (1998) 1410.
[13] P. Stangeby, et al., NF **55** (2015) 093014.

Figure Captions

Fig. 1. Typical results from the BALOO code. Pressure gradient stability boundary as a function of normalized poloidal flux, ψ (a), and shear versus the pressure gradient curves for individual flux surfaces nearest the separatrix (b). The curves in (b) yield a slightly lower stability bound that obtained in (a).

Fig. 2. Plot of the measured pressure gradient (solid symbols) and the BALOO calculated critical pressure gradient (open circles and squares: stability limits obtained from Figs. 1a and 1b respectively) as a function of $\beta_{p,omp}$.

Fig. 3. Comparison a tanh and hyperbola fits to the T_e data. The separatrix locations obtained by means of methods 2, 4, and 6 are indicated and are within +/- 2 mm of another. Substantially different gradients can be obtained dependent on both fit and separatrix location.

Fig. 4. Plots separatrix locations from methods 2-6 versus method 1, the standard method. The color-coding is red circles, blue squares, magenta circles, cyan squares, and green triangles for methods 2-6 respectively. There is a linear relationship between any two methods, each with a slope ~1, but differing in offset. The offset systematically shifts the separatrix for a particular method to higher or lower values, preserving the linear relationship between ∇P and $\beta_{p,omp}$ of Fig. 2.

Fig. 5. Plots of the electron (red circles) and ion (green squares) pressure versus the total pressure (a), and the 4 components of the pressure gradient ($n_e \nabla T_e$ (red circles), $T_e \nabla n_e$ (green squares), $n_i \nabla T_i$ (blue upward pointing triangles), and $T_i \nabla n_i$ (cyan downward pointing triangles)) versus the total pressure (b). The terms proportional to T_i are dominant.

Fig. 6. Plots of $\tilde{\alpha}_{SOL}$ versus the Greenwald fraction, f_{GW} showing $\tilde{\alpha}_{SOL}$ increasing with f_{GW}, with an abrupt increase at $f_{GW} \sim$ 4-5 (a) and of $\tilde{\alpha}_{HD}$ versus α_{efit}, the normalized separatrix pressure gradient obtained from a kinetic EFIT reconstruction. The data in (b) is well approximated by the relation $\tilde{\alpha}_{HD} \approx \alpha_{efit} / 2$.

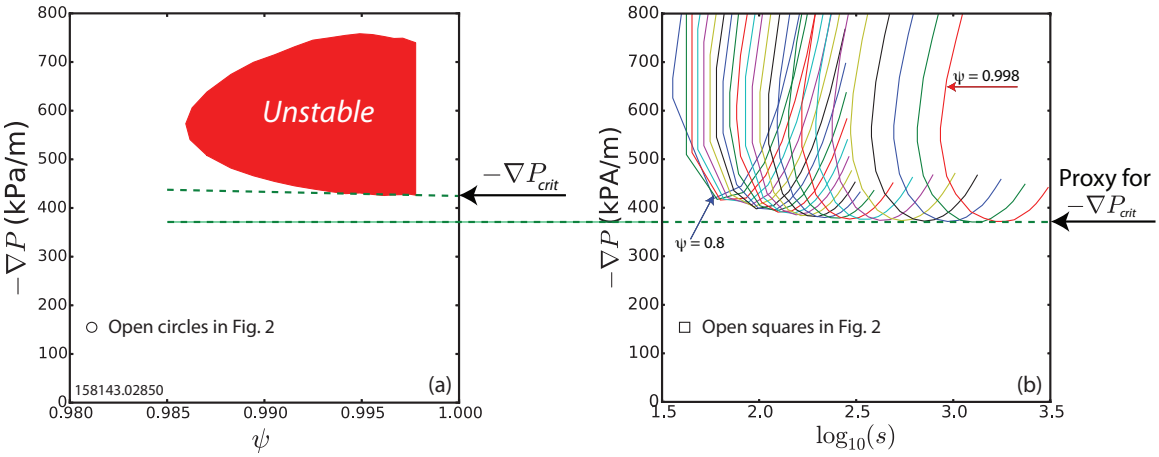
Unstable
$-\nabla P_{crit}$
$-\nabla P$ (kPa/m)
○ Open circles in Fig. 2
158143.02850
(a)
ψ
ψ = 0.998
ψ = 0.8
Proxy for
$-\nabla P_{crit}$
$-\nabla P$ (kPA/m)
□ Open squares in Fig. 2
(b)
$\log_{10}(s)$

Figure 1

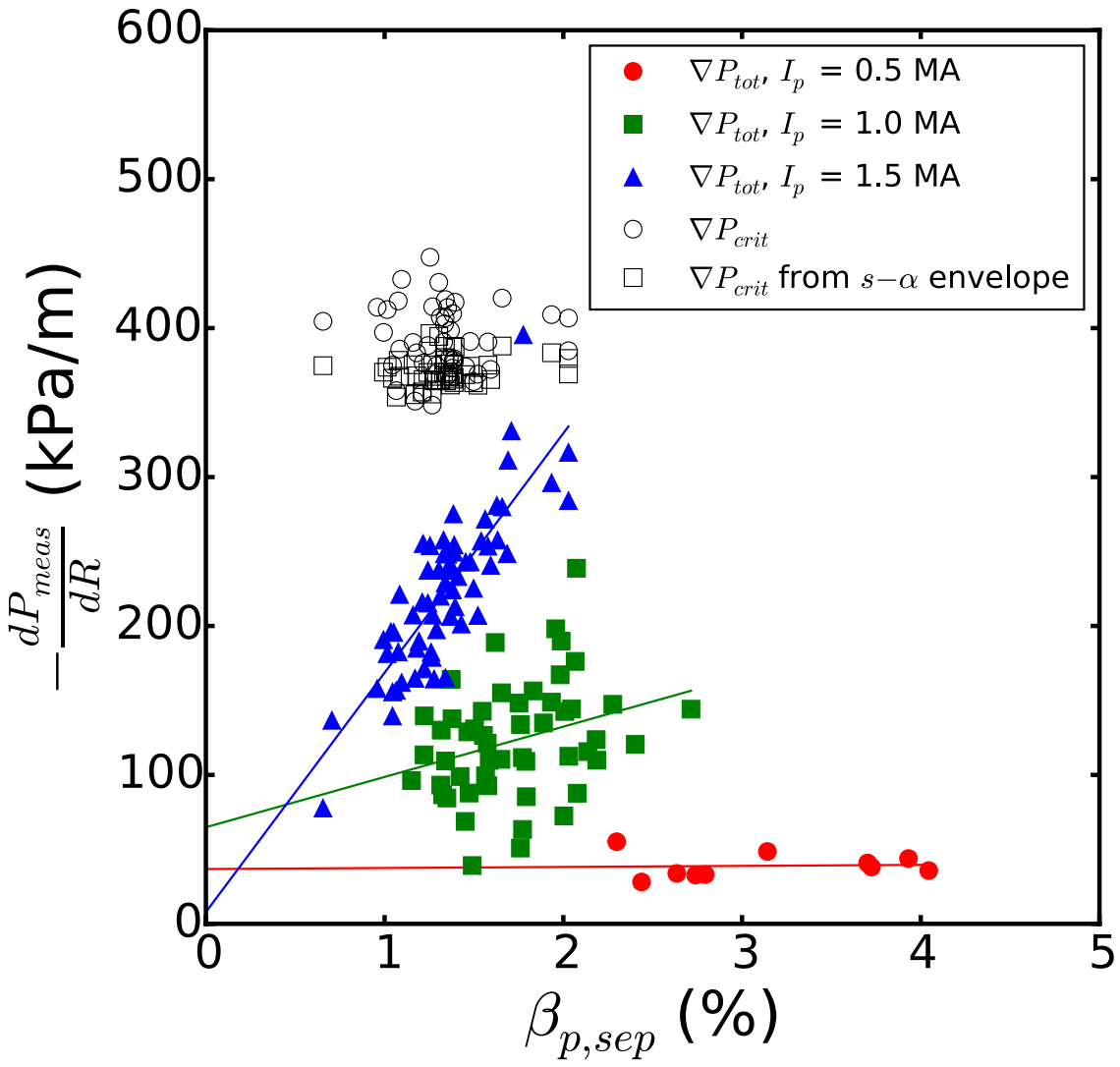
600
500
400
300
200
100
0
0
1
2
3
4
5
$-\frac{dP_{meas}}{dR}$ (kPa/m)
$\beta_{p,sep}$ (%)
∇P_{tot}, I_p = 0.5 MA
∇P_{tot}, I_p = 1.0 MA
∇P_{tot}, I_p = 1.5 MA
∇P_{crit}
∇P_{crit} from $s-\alpha$ envelope

Figure 2

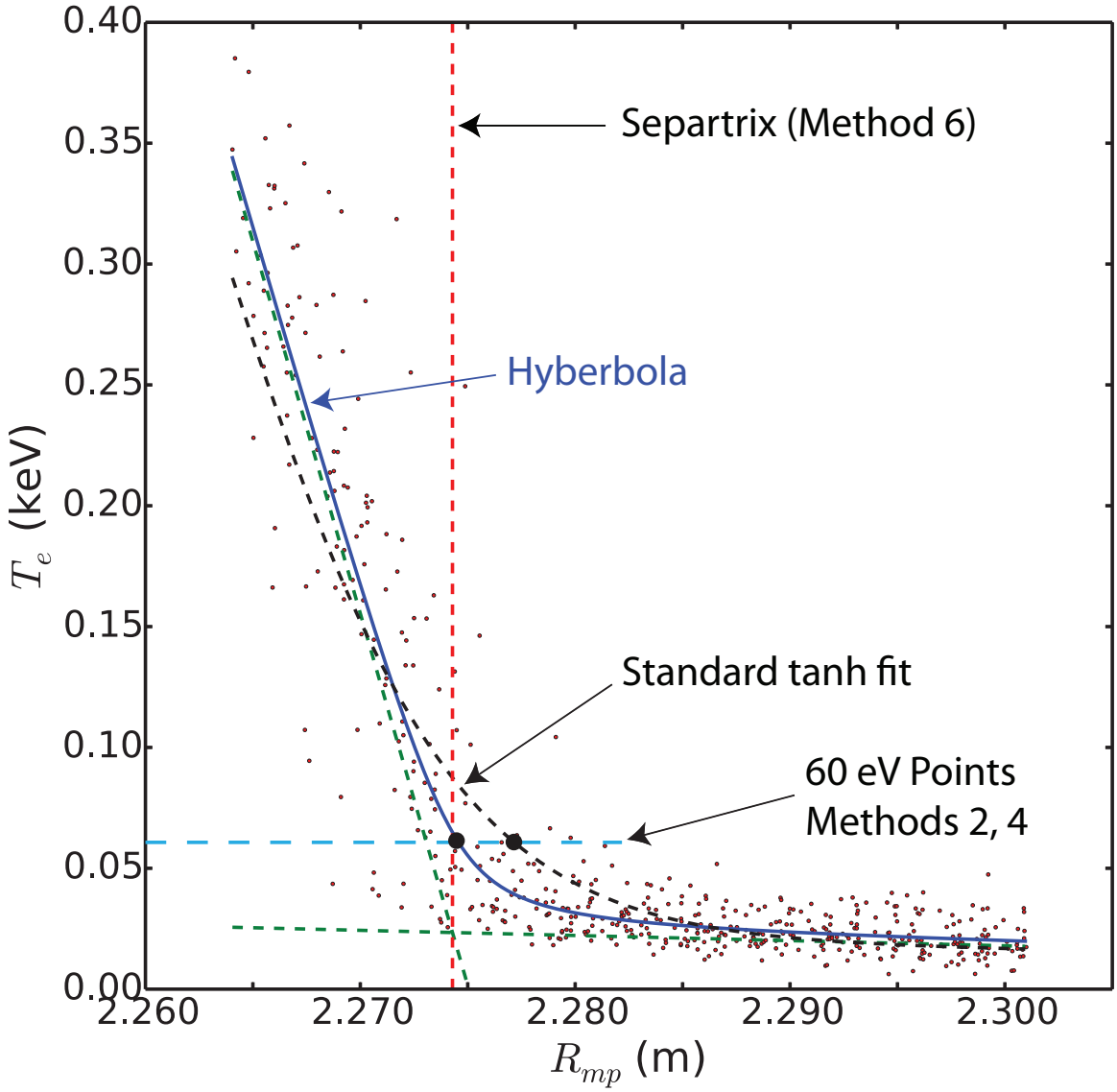
0.40
0.35
0.30
0.25
0.20
0.15
0.10
0.05
0.00
T_e (keV)
2.260
2.270
2.280
2.290
2.300
R_{mp} (m)
Separtrix (Method 6)
Hyberbola
Standard tanh fit
60 eV Points
Methods 2, 4

Figure 3

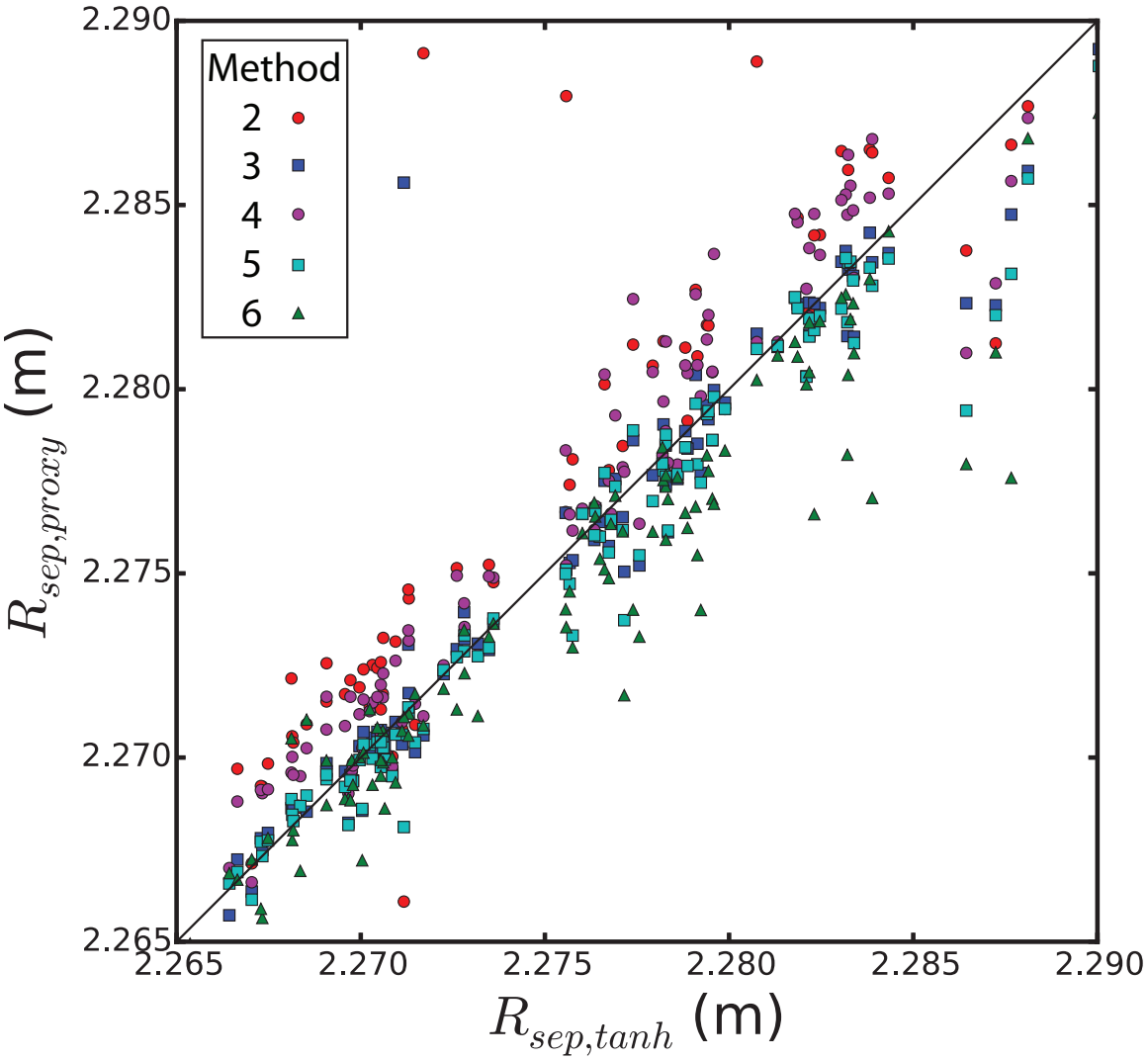
Method
2
3
4
5
6
2.290
2.285
2.280
2.275
2.270
2.265
2.265
2.270
2.275
2.280
2.285
2.290
$R_{sep,proxy}$ (m)
$R_{sep,tanh}$ (m)

Figure 4

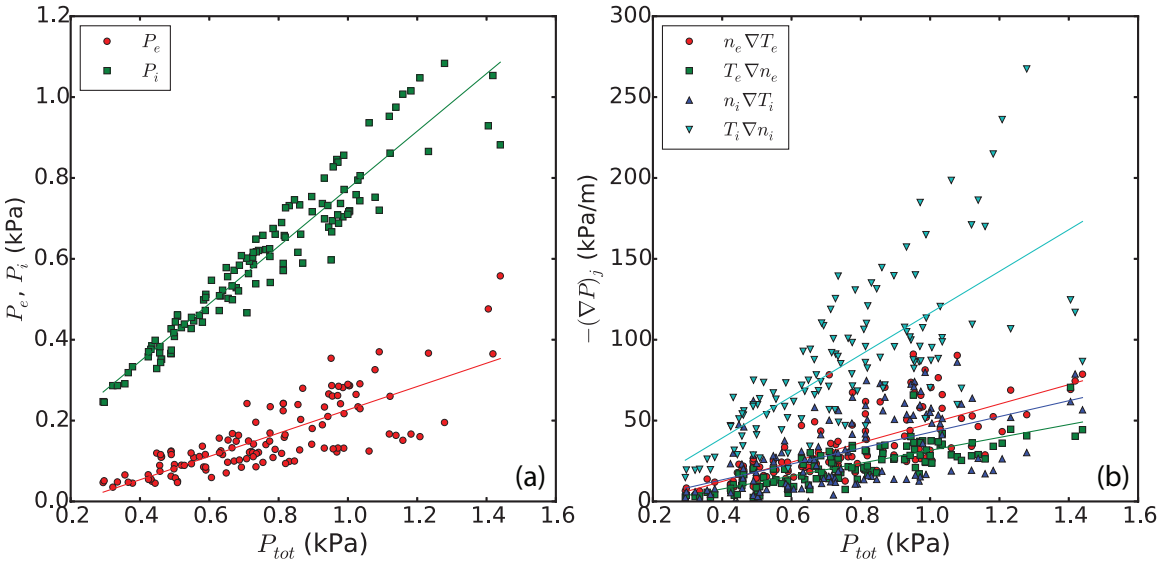
P_e
P_i
P_e, P_i (kPa)
P_{tot} (kPa)
(a)
$n_e\nabla T_e$
$T_e\nabla n_e$
$n_i\nabla T_i$
$T_i\nabla n_i$
$-(\nabla P)_j$ (kPa/m)
P_{tot} (kPa)
(b)

Figure 5

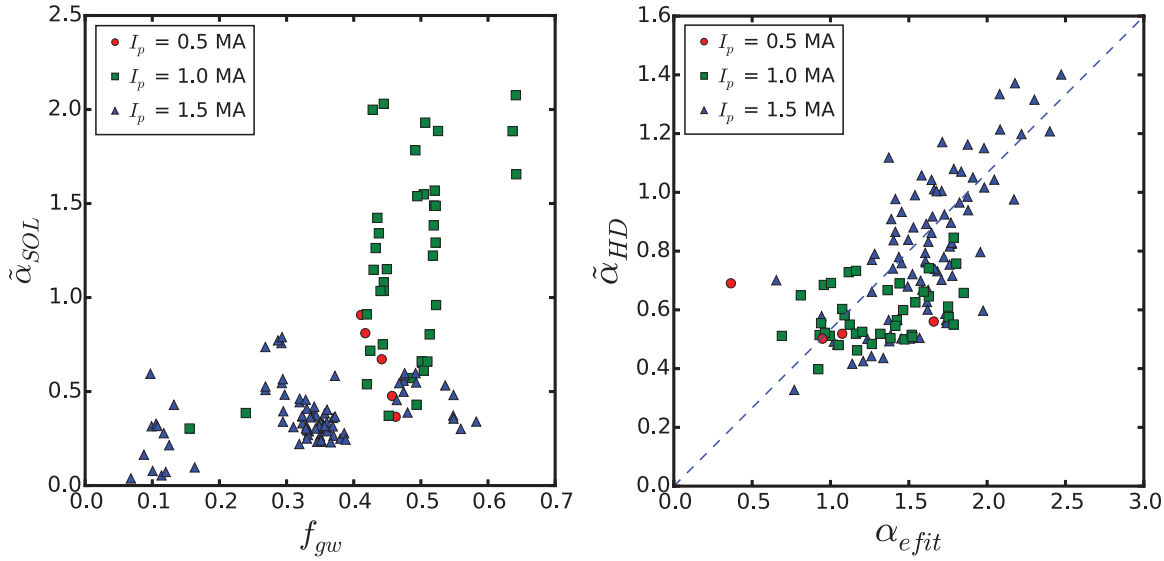
I_p = 0.5 MA
I_p = 1.0 MA
I_p = 1.5 MA
$\tilde{\alpha}_{SOL}$
f_{gw}
$\tilde{\alpha}_{HD}$
α_{efit}

Figure 6